# Nonlinear Saturation Behaviors of High-Speed p-i-n Photodetectors

Yong-Liang Huang and Chi-Kuang Sun, *Member, IEEE, Member, OSA*

***Abstract*—We present numerical simulations of the ultrafast transport dynamics in an ultrahigh-speed double-heterostructure p-i-n photodetector. Nonlinear saturation behaviors under high field and high power illumination are investigated with the external circuit response considered. Damping constants and diffusion constants are both treated as electric-field- and carrier-concentration-dependent in our model in order to take into account the effect of carrier scattering. We have also considered the carrier trapping at the heterostructure interfaces for the first time. Besides the drift-induced space charge screening effect, we find that saturation of external circuit and carrier-trapping-induced screening effect are also the dominant mechanisms contributed to the nonlinear bandwidth reduction under high power illumination. On the other hand, previously reported plasma oscillations are found to be greatly suppressed by including strong carrier diffusion effect in the model.**

***Index Terms*—Carrier trapping, high-speed photodetector, nonlinear saturation, p-i-n, plasma oscillation, space charge screening.**

## I. Introduction

DEVELOPMENT of high-speed and high-sensitivity photodetectors operating at 1.3–1.55-$\mu$m wavelengths is fundamental for new high-bit-rate long-wavelength optical communication systems. Ultrahigh bandwidth operation requires a thin absorption layer and a small active area in order to reduce the carrier transit time and detector RC time constant [1]. The small active volume results in a high carrier concentration and a high field. Under high power illumination, nonlinear saturation induced bandwidth reduction was observed experimentally [2], [3], which was tentatively attributed to the carrier-drift-induced space charge effect.

In this paper, we present a numerical simulation on the ultrafast transport dynamics of an ultrahigh-speed long-wavelength p-i-n photodetector. The device we modeled is an InP–InGaAs–InP double heterostructure backside illuminated detector [4]. The active region thickness is 180 nm, which allows a fast intrinsic response. In order to reduce the junction capacitance, the diameter of the active area is 2 $\mu$m. The fabricated device has demonstrated a record bandwidth of 120 GHz for the telecommunication wavelength [4].

Numerical simulations of numerous high-speed p-i-n photodetector structures have been previous reported by several research groups [5]–[8] including Dentan and Cremoux [5], Parker [6], and Ueda *et al.* [7]. Recently, Williams and his coworkers presented one of the most complete model [8], considering the effects of field-dependent-drift velocity, field-dependent-diffusion, and external load resistance. The analysis was performed in the frequency domain. The analyzed device active area thickness was on the order of 1 $\mu$m. The p-region absorption and carrier-dependent velocities associated with a perturbed electric field were shown to be the dominant photodetector nonlinear behavior [8]. In our study, we have not only analyzed the carrier transport in the time domain for the ultrathin device by solving three coupled nonlinear differential equation, including Poisson's equation, carrier continuity equation, and carrier motion equation under a high electric field, but have also considered carrier trapping at the heterostructure interfaces and the external circuit effect, including not only load resistance, but also device and parasitic capacitances. In order to take into accounts the carrier scattering and electric-field dependent effects, we have also considered electric-field- and carrier-density-dependent diffusion constants and damping constants, electric-field- and carrier-density-dependent carrier velocity, velocity-dependent trapping constant and bias-dependent depletion length. Sha and Smirl have previously observed coherent plasma oscillation at 80 K [9] in a GaAs p-i-n structure. Ueda *et al.*have also reported a plasma oscillation behavior in their numerical simulation [7]. We have studied plasma oscillation in our simulation with room temperature parameters. We find that the plasma oscillation in a p-i-n photodetector should be strongly suppressed by carrier diffusion at room temperature.

## II. Device Model

The doping densities of the simulated InP–InGaAs–InP double heterostructure p-i-n photodiode [4] in the n region and the p region are $3\times10^{18}$ cm$^{-3}$ and $2\times10^{18}$ cm$^{-3}$, respectively. We assume that the background carrier concentration in the intrinsic region is $1\times10^{16}$ cm$^{-3}$. The circuit model is shown in the inset of Fig. 1. The device is under reverse bias. In the circuit model, we have considered a parasitic capacitance $C_p$ of 4 fF, a photodiode resistance $R_{\rm pd}$ of 65 $\Omega$, and a load resistance $R_L$ of 50 $\Omega$. These parameters are taken from the measurements of the physical device [4]. The calculated dark electric field under a 2-V reverse bias is shown in Fig. 1. The dielectric constants for InP and InGaAs are 12.4 and 13.77, respectively [10]. We have taken the dielectric constant as 13.77 for the whole region so the dark electric field in Fig. 1 is continuous.

Manuscript received February 8, 1999; revised August 24, 1999. This work was supported by National Science Council of Taiwan, R.O.C., under Grant NSC-88-2218-E-002-038.

The authors are with the Department of Electrical Engineering and Graduate Institute of Electro-Optical Engineering, National Taiwan University, Taipei, Taiwan 10617, R.O.C. (e-mail: sun@cc.ee.ntu.edu.tw).

Publisher Item Identifier S 0733-8724(00)01310-4.

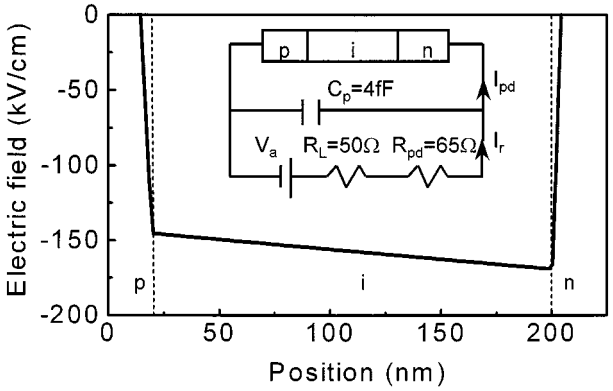


Fig. 1. Dark electric field distribution under a 2-V reverse bias. Inset shows the photodetector circuit model.

## III. Mathematical Method

### A. Transport Equations

The basic equations governing the carrier behaviors are the Poisson's equation, the carrier motion equations, and the carrier continuity equations. By neglecting the transverse variation, the one-dimensional (1-D) Poisson's equation is described in the following form:

$$\frac{\partial^2}{\partial z^2}V_{\rm sc}(z,t)=\frac{e}{\varepsilon}[n(z,t)-p(z,t)] \tag{1}$$

where $V_{\rm sc}(z,t)$ is the built-in potential formed by photogenerated electrons and holes, $e$ is the value of electron charge, $n(z,t)$ and $p(z,t)$ are the excess electron and hole densities generated by photoexcitation. $z$ and $t$ are longitudinal position and time. The space charge field $E_{\rm sc}$ can then be obtained from the relation of $E_{\rm sc}(z,t)=-(\partial V_{\rm sc}(z,t))/\partial z$.

The continuity equations are described by

$$\frac{\partial}{\partial t}n(z,t)=D_n\frac{\partial^2}{\partial z^2}n(z,t)-\frac{\partial}{\partial z}[n(z,t)v_n(z,t)] \tag{2}$$

$$\frac{\partial}{\partial t}p(z,t)=D_p\frac{\partial^2}{\partial z^2}p(z,t)-\frac{\partial}{\partial z}[p(z,t)v_p(z,t)]. \tag{3}$$

While the first term in the continuity equations describes the carrier diffusion, the second term is due to the carrier drift under an electric field. $D_n$ and $D_p$ are the electron and hole diffusion constants. The diffusion constants are functions of velocity and electric field, which will be given in Section III-B. $v_n(z,t)$ and $v_p(z,t)$ are electron and hole velocities. For an InP–InGaAs–InP heterostructure p-i-n photodetector, there exist a barrier height of 0.16 eV at the i–p interface and a barrier height of 0.12 eV at the i–n interface. We introduce a carrier trapping term to simulate this effect. We assume that carriers can not pass these barriers by drift or diffusion. The trapping time constant is a function of the carrier kinetic energy. The continuity equations of carriers at the heterostructure interfaces are described in the following forms:

$$\frac{\partial}{\partial t}n(z,t)=-\frac{n(z,t)}{\tau_n} \tag{4}$$

$$\frac{\partial}{\partial t}p(z,t)=-\frac{p(z,t)}{\tau_n} \tag{5}$$

with

$$\tau_n=\tau_{n0}/\exp\left(\frac{1}{2}m_nv_n^2/kT\right) \tag{6}$$

$$\tau_p=\tau_{p0}/\exp\left(\frac{1}{2}m_pv_p^2/kT\right). \tag{7}$$

$\tau_n$ and $\tau_p$ are the carrier trapping times for kinetic electrons and holes. $m_n$ and $m_p$ are the electron and hole effective masses. $\tau_{n0}$ and $\tau_{p0}$ are given carrier trapping constants.

The motion equations for electrons and holes in the presence of electric field are given by the following equations:

$$m_n\frac{\partial}{\partial t}v_n(z,t)=-eE-\alpha_nv_n(z,t) \tag{8}$$

$$m_p\frac{\partial}{\partial t}v_p(z,t)=+eE-\alpha_pv_p(z,t). \tag{9}$$

$E$ is the total electric field across the device. $\alpha_n$ and $\alpha_p$ are the damping constants of electrons and holes. The damping constants are functions of velocity and electric field as given in the Section III-B.

Under photoillumination, electron-hole pairs are generated in the depletion region [5] with $G_i = G_0\{\exp(-\alpha z)+\exp(-\alpha Z)\exp[-\alpha(L-z)]\}$, where $G_0$ is a constant, $L$ is the active layer thickness, and $\alpha=10\,000\ {\rm cm}^{-1}$ is the optical absorption coefficient [5]. The first term describes the absorption of incident beam and the second term describes the absorption of the reflected beam. An average carrier concentration is used in this text to indicate the above described carrier distribution that will be used in our simulation.

### B. Nonlinear Properties

There is a nonlinear relation between the carrier drift velocity and the electric field due to the Gunn effect [11], [12]. However a well-defined formula is not available. According to research of Haase *et al.*[13], we can find the peak threshold velocity and the corresponding threshold electric field for a given carrier concentration. By choosing proper parameters we can then approximate the steady-state velocity-field relationship according to the experimental formulas [5]. Fig. 2(a) presents velocity-field relations for a carrier concentration of $1\times10^{17}\ {\rm cm}^{-3}$, given by the following approximated equations:

$$V_e(E,\mu_n,\gamma)=(\mu_n|E|+\beta V_{nl}|E|^\gamma)/(1+\beta|E|^\gamma) \tag{10}$$

$$V_h(E,\mu_p)=V_{pl}\tanh(\mu_p|E|/V_{pl}). \tag{11}$$

$V_e$ and $V_h$ are velocities of electrons and holes in steady state for a given carrier concentration and electric field. $\beta=7.4\times10^{-10}$, $V_{nl}=6\times10^6\ {\rm cm\cdot s^{-1}}$, and $V_{pl}=4.8\times10^6\ {\rm cm\cdot s^{-1}}$. $\mu_n$ and $\mu_p$ are electron and hole mobilities under low

TABLE I
$\mu_n$ AND $\gamma$ FOR DIFFERENT CARRIER CONCENTRATIONS.

| n | $n<10^{16}$ | $10^{16}cm^{-3} \leqq n \leqq 10^{17}cm^{-3}$ | $10^{17}cm^{-3} \leqq n \leqq 10^{18}cm^{-3}$ | $n>10^{18}$ |
|---|---|---|---|---|
| $\mu_n$ | 14000 | 14000+(12000-14000)(n – $10^{16}$)/($10^{17}$-$10^{16}$) | 12000+(7600-12000)(n- $10^{17}$)/( $10^{18}$-$10^{17}$) | 7600 |
| $\gamma$ | 2.63 | 2.63+(2.6-2.63) (n - $10^{16}$)/( $10^{17}$-$10^{16}$) | 2.6+(2.54-2.6)(n - $10^{17}$)/( $10^{18}$-$10^{17}$) | 2.54 |

electric field. In steady state, carrier velocity and electric field are related by $V_e = \mu_n E$ and $V_h = \mu_p E$ under low field. In order to take the carrier scattering effect into consideration, we have linearly approximated the electron mobility for carrier concentration among $1 \times 10^{16}$ cm$^{-3}$ and $1 \times 10^{18}$ cm$^{-3}$ from the previously published data [13]. The parameter $\gamma$ is approximated in the same way. The values of $\mu_n$ and $\gamma$ are listed in Table I. Pearsall *et al.* [14] found that the hole mobility is approximately proportional to the electron mobility with $(\mu_n/\mu_p)_{T=295\,\mathrm{k}} = 25$, so that we can then deduce the hole mobility with this relation. Under large electric field, saturation velocities for electrons and holes are taken as $6.4 \times 10^6$ cm/s and $4.8 \times 10^6$ cm/s. Electric-field-dependent and carrier-velocity-dependent damping constants and diffusion constants can then be obtained. In steady state, left sides of (8) and (9) are zero. We can then deduce the values of the damping constants as $\alpha_n = |(eE)/V_e|$ and $\alpha_p = |(eE)/V_h|$, where $E, V_e$ and $V_h$ are given by (10) and (11). According to (10) and (11), the value of the damping constant is proportional to magnitude of the electric field.

As the magnitude of the electric field increases, there is also a nonlinear relation between the diffusion coefficient and the field [15]. However there is no simple formula available. We approximate the field-dependent diffusion constants by using the Einstein relation and (10) and (11) with

$$D_n = \frac{kT}{e} \cdot \left| \frac{V_e}{E} \right| \tag{12}$$

$$D_p = \frac{kT}{e} \cdot \left| \frac{V_h}{E} \right|. \tag{13}$$

$k$ is the Boltzmann constant and $T$ is the absolute temperature. For a carrier concentration of $1 \times 10^{17}$ cm$^{-3}$, the electron and hole diffusion constants are shown in Fig. 2(b) as an example. We can find that the electron diffusion constants under low field are much greater than those under high field.

### C. Current Calculation

*1) Equation Derivation:* The carrier continuity equation includes a drift term and a diffusion term. The conduction current $I_c$ in the device is thus described by both the drift current density $J_{\mathrm{drift}}$ and the diffusion current density $J_{\mathrm{diff}}$ as

$$I_c(t) = [J_{\mathrm{drift}}(t) + J_{\mathrm{diff}}(t)] \cdot A \tag{14}$$

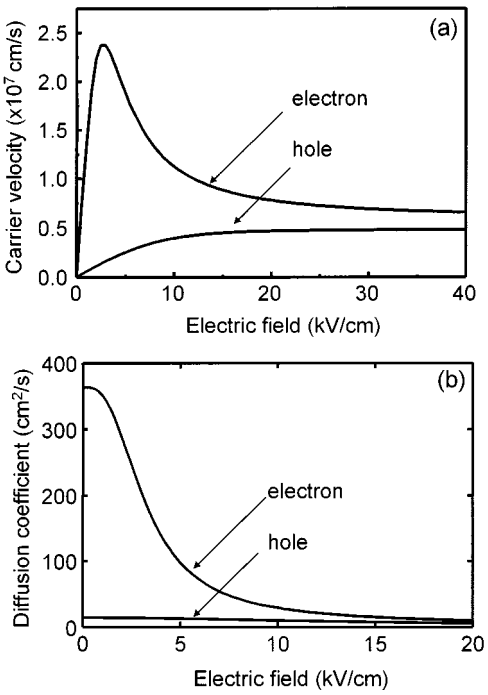


Fig. 2. (a) Field dependent steady-state carrier velocities for a carrier concentration of $1 \times 10^{17}$ cm$^{-3}$. (b) Field-dependent diffusion coefficients.

with

$$J_{\mathrm{drift}}(t) = e \cdot v_n(z,t) n(z,t) - e \cdot v_p(z,t) p(z,t) \tag{15}$$

$$J_{\mathrm{diff}}(t) = -e \cdot D_n \frac{\partial}{\partial z} n(z,t) + e \cdot D_p \frac{\partial}{\partial z} p(z,t). \tag{16}$$

$A$ is the device area and $I_c$ is calculated at the edge of the depletion region near the p region. When carriers flow out of the depletion region, the electric neutrality is no longer maintained due to different drift velocities of electron and hole. Free charges are then accumulated on the edges of the depletion region with an induced electric field and potential. The electric field in the depletion region and potential across the depletion region can be described by [5]

$$E(z,t) = E_{\mathrm{dark}} - E_j(t) + E_{\mathrm{sc}}(z,t) \tag{17}$$

with

$$E_j(t) = Q(t)/(\varepsilon \cdot A) \tag{18}$$

and

$$V = V_{\rm dark} + Q(t)/C_j + V_{\rm sc}. \tag{19}$$

$E_j$ is the junction capacitance field induced by the accumulated free charges $Q(t)$ on the depletion edge of the p region. $C_j$ is the junction capacitance across the depletion region. A displacement current is also induced due to the variation of $Q(t)$ in a very short time $dt$ with

$$I_d(t) = \frac{dQ(t)}{dt}. \tag{20}$$

*2) Current Calculation of the Circuit:* The circuit model is shown in the inset of Fig. 1. $V_a$ is the applied reverse bias voltage. $I_r$ is the current flowing through the resistance. $I_{\rm pd}$ is the current flowing into the photodetector. Potential across the device can be given in the following form:

$$\frac{Q(t)}{C_j} + V_{\rm sc}(t) = \frac{Q_c(t)}{C_p} \tag{21}$$

where $Q_c(t)$ is the excess charge stored in the parasitic capacitor $C_p$. Combining (20) and (21) the displacement current is given as [5]

$$I_d(t) = -\left[\frac{Q(t)}{C_j} + V_{\rm sc}(t) + RC_p\frac{dV_{\rm sc}(t)}{dt} + RI_c(t)\right] \cdot \frac{C_j}{R(C_p + C_j)} \tag{22}$$

where $R = R_L + R_{\rm pd}$ is the total resistance. The electric charge $Q(t)$ can be obtained by

$$Q(t) = \int I_d(t)\, dt. \tag{23}$$

The current flow through the parasitic capacitance $C_P$ is given by

$$I_{\rm cp}(t) = \frac{dQ_c(t)}{dt}. \tag{24}$$

The total current flowing into the photodetector $I_{\rm pd}$ is the summation of the displacement current and the conduction current,

$$I_{\rm pd}(t) = I_d(t) + I_c(t). \tag{25}$$

The current flowing through the resistance $R$ is given by

$$I_r(t) = I_{\rm pd}(t) + I_{\rm cp}(t). \tag{26}$$

## IV. Numerical Method

Finite difference numerical technique is used in the simulation. A flowing chart to calculate the current response is given in Table II. The initial value of $Q(t)$ and $E_{\rm sc}(z,t)$ is zero at $t = 0$. The total electric field is then obtained by (17) and is used to calculate the field-dependent diffusion and damping constants according to (10) and (11). Carrier velocities are calculated from motion equations (8) and (9). Velocity-dependent trapping constants are then obtained from (6) and (7). Continuity equations (2) and (3) are then used to calculate the distribution of carrier concentration in the depletion region. The current responses $I_c$, $I_d$, $I_{\rm pd}$ and $I_r$ are obtained by (14), (22), (25), and (26) respectively. The accumulated excess charge $Q(t)$ is obtained by (23). 3 dB frequency can be finally obtained by applying fast Fourier transforms (FFT's) to the simulated current impulse response $I_r$. Parameters used in the model are given in Table III.

## V. Simulation Result

### A. Internal Behavior

Under high power illumination, nonlinear bandwidth saturation of ultrahigh speed p-i-n devices was observed and attributed to the carrier-drift-induced space charge screening effect [2], [3]. When carriers drift under reverse bias, space charge field is induced. The induced field is in the opposite direction to the bias electric field and the total electric field becomes smaller. With a total field close to zero, the carrier drift velocities become much lower and a slow current response is then expected, which would result in the observed bandwidth reduction. In order to understand the contribution of drift-induced space charge screening effect, we have investigated this internal behavior by neglecting the external circuit components. The voltage across the photodiode is thus kept as the bias voltage $V_a$. resistance–capacitance (RC) time constant, which will limit the unsaturated response function, is thus also neglected. In order to make the drift-induced space charge screening effect the only factor contributed to the saturation behavior, we have also neglected the carrier trapping effect. The simulated internal responses for two different photocarrier concentrations are shown in Fig. 3(a) and (b) with a reverse bias of 2 V. For a photocarrier concentration of $1 \times 10^{17}$ cm$^{-3}$ as shown in Fig. 3(a), the induced space charge field is small with carriers moving at the saturation velocities. The observed current response has a drift-time-limiited 3-dB bandwidth of 151 GHz. For a higher carrier concentration of $7 \times 10^{17}$ cm$^{-3}$, the drift-induced space charge field starts to screen out the bias field after $\sim$1 ps. A sharp decrease and a long tail in the current response can thus be observed as shown in Fig. 3(b). The corresponding saturated 3-dB bandwidth is $\sim$121 GHz. Fig. 4 shows the simulated 3-dB bandwidth (open diamonds) for different photocarrier concentrations. Experimental data [3] is also shown as solid circles for comparison. As shown in Fig. 4, the calculated 3-dB bandwidth by this internal model presents a large deviation from the experimental observation. The simulated threshold carrier density for bandwidth saturation is much higher than experimental data, indicating the existence of other dominating mechanisms responsible for the observed nonlinear bandwidth reduction.

### B. External Circuit Behavior

We have considered the external circuit response according to the inset of Fig. 1, which will affect both the unsaturated bandwidths (due to the RC time constant) as well as the saturated bandwidth. In order to compare the effect of carrier trapping, we have neglected the trapping effect at this moment. For a low concentration of $1 \times 10^{17}$ cm$^{-3}$ under a 2-V reverse bias, carriers are moving with saturation velocities and the response described in Section V-A is only modified by the external circuit RC response as shown in Fig. 3(a). A 3-dB bandwidth of 121

TABLE II
FLOWING CHART OF THE NUMERICAL CALCULATION.

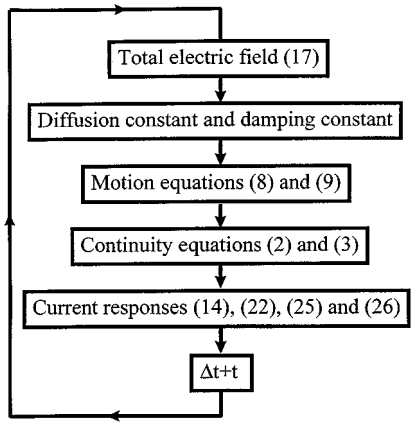


TABLE III
DEVICE PARAMETERS USED IN THE SIMULATION.

| | |
|---|---|
| p region doping density | $P^+ = 2x10^{18}$ cm$^{-3}$ |
| i region doping density | $P^- = 1x10^{16}$ cm$^{-3}$ |
| n region doping density | $N^- = 3x10^{18}$ cm$^{-3}$ |
| Electron effective mass [16] | $m_n = 0.041m_0$ |
| hole effective mass [10] | $m_p = 0.62m_0$ |
| Active region diameter | 2 μm |
| Photodetector resistance | $R_{pd}$=65 Ω |
| load resistance | $R_L$=50 Ω |
| Junction capacitance | $C_j$ = 2.17 fF |
| Parasitic capacitance | $C_p$ = 4 fF |
| Temperature | T=300 K |
| dielectric constant [10] | $\varepsilon = 13.77\varepsilon_0$ |
| Active length | $L_0$=180 nm |
| dt with diffusion term neglected | Δt =0.3 fs~0.8 fs |
| dt with diffusion term considered | Δt=0.05 fs |
| Space interval | Δx=1.9 nm |
| applied external voltage | $V_a$=-2.0 V |
| Depletion length under 2V bias | 189 nm |

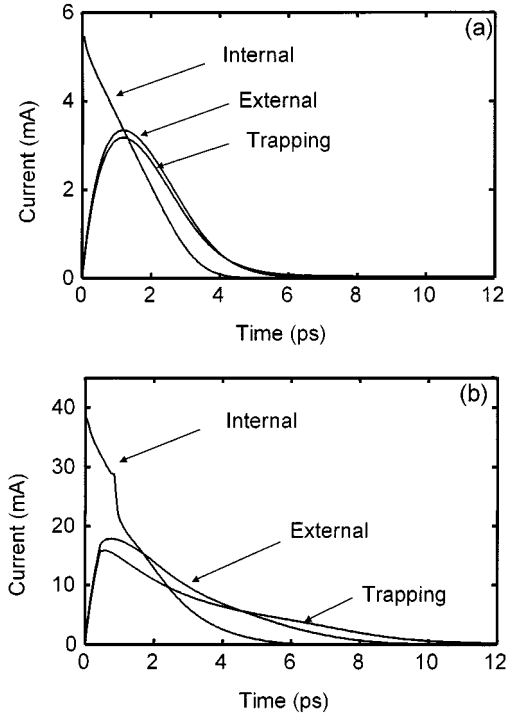


Fig. 3. External circuit current response $I_r$ under a 2-V reverse bias for different simulation models with photocarrier concentrations of (a) $1 \times 10^{17}$ cm$^{-3}$ and (b) $7 \times 10^{17}$ cm$^{-3}$.

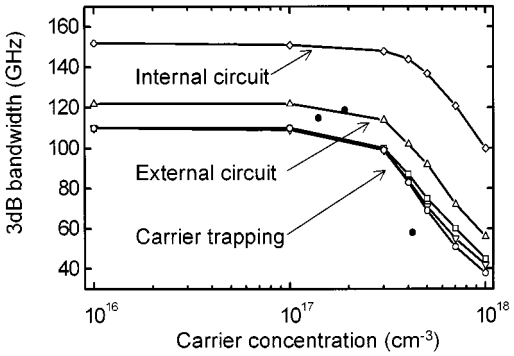


Fig. 4. A 3-dB bandwidth versus photocarrier concentration under a 2-V reverse bias for the internal model (open diamond), the external circuit model neglecting trapping (open triangle), and the external circuit model considering trapping with $\tau_{n0} = 1.25$ ps (open square), 2.5 ps (open inverted triangle), and 5 ps (open circle). Experimental data from [3] are also shown as solid circles for comparison.

GHz and a full-width at half-maximum (FWHM) current response of 2.65 ps can be obtained, which are in excellent agreements with the experimental data. With a photocarrier concentration of $7 \times 10^{17}$ cm$^{-3}$, the simulated bandwidth reduces to 72 GHz, which is shown in Fig. 3(b). The drift-induced space charge effect and RC time constant can not completely explain this large bandwidth reduction. We attribute the observed extra bandwidth reduction to external circuit saturation. With an ultrafast response, the resulted large transient peak current flowing in the resistance would induce a large voltage drop, which reduces the applied bias and the electric field across the depletion region and results in the slow current response shown in Fig. 3(b). The simulated 3-dB bandwidth for different photocarrier concentrations have also been shown in Fig. 4 (open triangles). Please notice that we have considered junction capacitance (intrinsic in the model), parasitic capacitance, photodiode resistance, and load resistance, all with physically measured parameters [4]. Even though our simulation shows excellent agreement with measurements under low illumination, the simulated saturation responses under high illumination still exist a large difference from the experimental observations that exhibit a much lower saturation bandwidth.

### C. Carrier Trapping Effect

Due to the discrepancy observed in our simulation, we have thus considered the carrier trapping effect at the heterojunction interfaces. Equations (4) and (5) simulate the carrier trapping mechanism. Due to the difficulty to experimentally determine the actual trapping time, we have first assumed the trapping constants $\tau_{n0}$ and $\tau_{p0}$ as 5 and 10 ps. The real trapping time is much shorter than $\tau_{n0}$ and $\tau_{p0}$ according to (6) and (7). The effect of different trapping time will be discussed later. The simulated current responses for photocarrier concentrations of $1 \times 10^{17}$ cm$^{-3}$ and $7 \times 10^{17}$ cm$^{-3}$ under a 2-V reverse bias, including

both trapping and external circuit effects, are shown in Fig. 3(a) and (b). The corresponding 3-dB bandwidths are 111 GHz and 51 GHz, respectively. With a low carrier density in the unsaturated regime, the simulated results show that the carrier trapping effect does not delay the carrier drift time much as previously expected [4]. We thus do not observe any obvious bandwidth reduction under low illumination. This means that this trapping effect can be neglected in the low illumination model and most of the device bandwidth calculations have already adopted this simplification. However, with a high photocarrier density, this trapping effect does seriously cause bandwidth reduction. We attribute this effect to the space charge screening field created by the trapped carriers.

Fig. 5 shows the simulated carrier density and electric field distributions at $t = 1$ ps for the carrier concentration of $1\times10^{17}$ cm$^{-3}$. Due to the trapping effect, carriers are trapped at the interfaces and a space charge screening field $E_{\rm sc}$ is induced. The electric neutrality is destroyed and a large excess charge $Q(t)$ is induced to balance the variation, which sets up a junction electric field $E_j$ according to (18). From Fig. 5(b), the magnitude of the negative total field is slightly decreased in the middle depletion region and increased on the two sides. The carriers thus still move with saturation velocities. Fig. 6(a) and (b) shows the corresponding transient electron and hole density distributions. Most of the carriers have left the bulk in 4.0 ps with saturation velocities. The trapped carriers move away in a much longer time due to the large time constant we have adopted in this particular simulation. However they do not make any significant contribution to the external current response.

Fig. 7 shows the electric field and carrier velocity distributions at $t = 0.48$ ps for the higher carrier concentration of $7\times10^{17}$ cm$^{-3}$. The total electric field is close to or even greater than zero in the middle depletion region, mostly due to the trapping induced space charge field and partly due to the drift induced space charge field. While most holes move with a smaller velocity, it is interesting to notice that parts of the electrons change their moving directions due to the positive total electric field as shown in Fig. 7(b). Fig. 8 shows the corresponding transient electron and hole velocity distributions. Electrons and holes first move with saturation velocities of $6.4\times10^{6}$ cm/s and $-4.8\times10^{6}$ cm/s at time $t$ slightly greater than zero. As time increases, due to the setup of the strong space charge field, parts of the electron population starts to move at a slower speed or even change their moving directions. This behavior is similar to an underdamped plasma oscillation and will be further discussed later. As the carriers gradually leave the bulk, the total electric field recovers to be negative. The carriers then all move back to their original directions and finally move with the saturation velocity. Fig. 9 shows the corresponding transient electron and hole density distributions. Compared with Fig. 6, a much slower detector response can be observed.

Fig. 4 also shows the calculated 3-dB bandwidths with the electron trapping constant $\tau_{n0}$ as 1.25, 2.5, and 5 ps (as open squares, open inverted triangles, and open circles). The hole trapping constant $\tau_{p0}$ is kept as two times of $\tau_{n0}$ due to a larger hole effective mass and a larger barrier height at the i–p interfaces. While with low carrier densities the device bandwidth is reduced because of the delayed current response due to the carrier trapping time, with high carrier densities the bandwidth

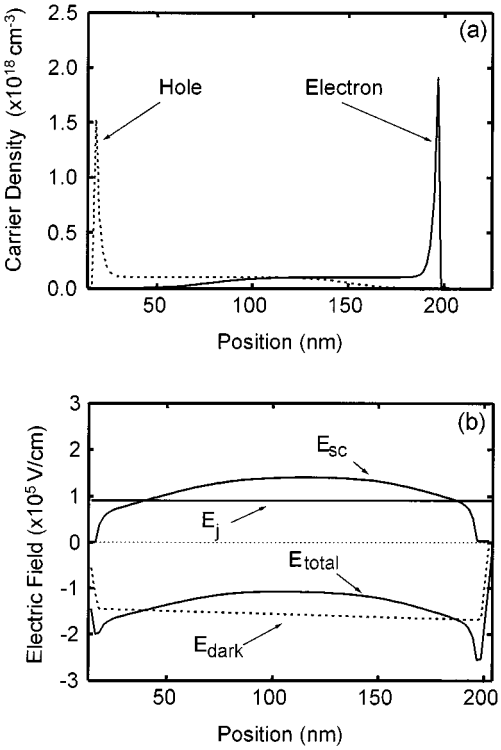


Fig. 5. (a) Carrier density distribution at $t = 1$ ps for a photocarrier concentration of $1\times10^{17}$ cm$^{-3}$ with trapping considered under a 2-V reverse bias. (b) Corresponding electric field distribution.

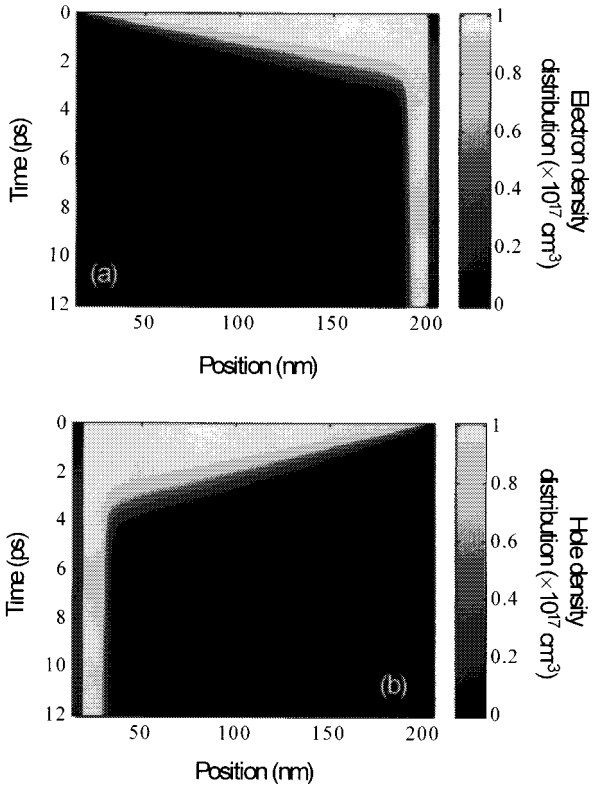


Fig. 6. (a) Transient electron density distribution with trapping considered for a photocarrier concentration of $1\times10^{17}$ cm$^{-3}$ under a 2-V reverse bias. (b) Corresponding transient hole density distribution.

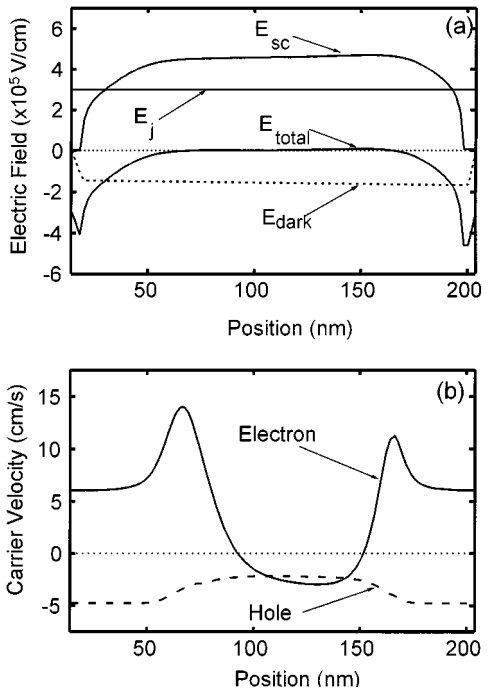


Fig. 7. (a) Electric field distributions at $t = 0.48$ ps for a photocarrier concentration of $7 \times 10^{17}$ cm$^{-3}$ under a 2-V reverse bias with trapping considered. (b) The corresponding carrier velocity distributions.

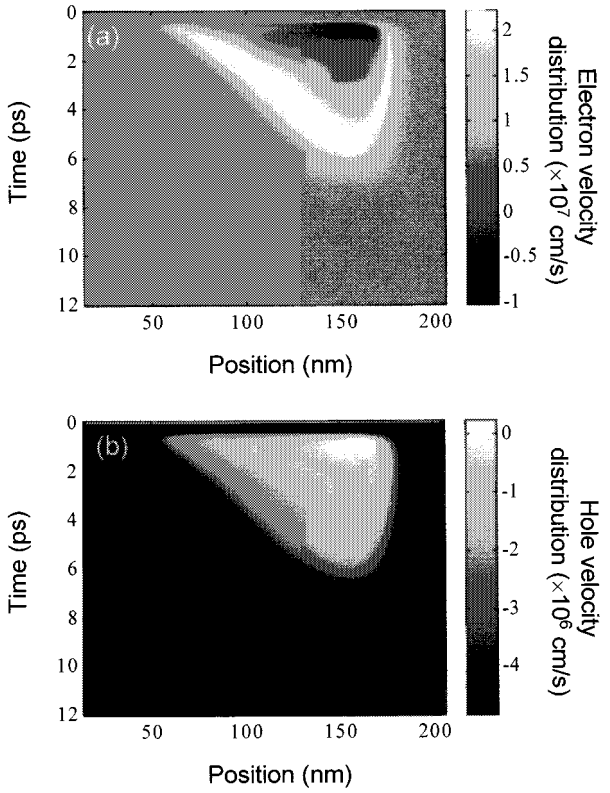


Fig. 8. (a) Transient electron velocity distribution with trapping considered for a carrier concentration of $7 \times 10^{17}$ cm$^{-3}$ under a 2-V reverse bias. (b) Corresponding transient hole velocity distribution.

was found to be strongly saturated due to the trapped carrier induced space charge field. The calculated 3-dB bandwidth can be reduced from 92 GHz (neglecting carrier trapping) to 75, 71,

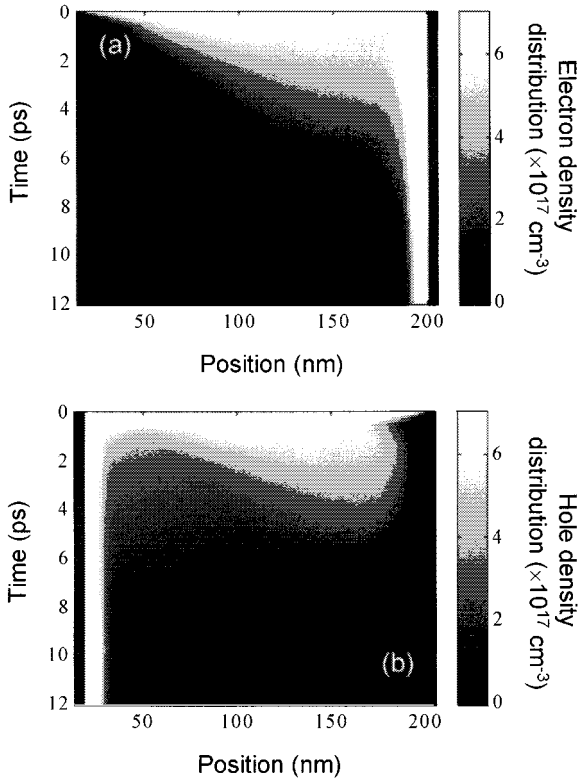


Fig. 9. (a) Transient electron density distribution with trapping considered for a photocarrier concentration of $7 \times 10^{17}$ cm$^{-3}$ under a 2-V reverse bias. (b) Corresponding transient hole density distribution.

or 69 GHz (with $\tau_{n0}$ of 1.25, 2.5, or 5 ps) for a carrier concentration of $5 \times 10^{17}$ cm$^{-3}$. These simulation results indicate that the carrier-trapping effect is one of the dominant factors for the bandwidth reduction under high power illumination and it thus should not be neglected. It is also interesting to notice that the different trapping constant does not change the bandwidth much. With all three effects considered, the simulation results now agree better with experimental data, indicating the importance of both external circuit saturation and trapping effects on the nonlinear bandwidth saturation of the ultrahigh-speed p-i-n photodetector.

### *D. Bias Dependent Response*

Previous experiments have shown that the nonlinear saturation behavior in the ultrahigh-speed p-i-n devices can be recovered by applying a higher external bias [3]. We have also studied the bias dependent nonlinear current response under high illumination in the simulated devices. For a carrier concentration of $7 \times 10^{17}$ cm$^{-3}$, current responses with different bias voltages are shown in Fig. 10. The 3-dB bandwidths for biased voltages of 1, 2, 3, 5, and 7 V are 37, 51, 66, 81, and 89 GHz, respectively. As bias increases, a higher photocarrier concentration is needed to create a space charge field large enough to screen out the applied bias field. A higher carrier concentration is also needed to create a larger transient peak current to saturate the external circuit. We thus observe a larger bandwidth as the bias voltage increase. When the bias voltage is larger than 7 V, the external circuit is completely recovered. The device bandwidth will then

be determined by the bias-dependent depletion width and RC time constant.

### *E. Plasma Oscillation*

Sha *et al.*have previously reported an observation of coherent plasma oscillation in a GaAs p-i-n structure at a cryogenic temperature of 80 K [9]. They have attributed the observation to the reduction of carrier-carrier scattering at low temperature. Ueda *et al.*have also reported a similar plasma oscillation in a GaAs p-i-n photodetector in a numerical simulation [7] with 77 K device parameters. They have observed a strong oscillation of the internal electric field at the midpoint of the device. No similar oscillation is observed in Fig. 8 of our simulation with 300 K parameters. We attribute the suppression of the plasma oscillation to the strong diffusion effect at room temperature instead of a strong carrier-carrier scattering.

By neglecting the carrier diffusion effect, Fig. 11(a) shows the simulated current response $I_{\rm pd}$ and the corresponding external circuit response $I_r$ for a photocarrier concentration of $7 \times 10^{17}$ cm$^{-3}$. The current response $I_{\rm pd}$ shows a strong oscillation that is filtered out in the external response by the slow RC time constant. This strong oscillation can be attributed to the plasma oscillation. It's interesting to notice that this oscillation can only be observed in the saturated responses. Due to the facts that the effective mass and damping constant of electrons are much smaller than those of holes, electron should be the dominant carrier type in the plasma oscillation. Electron plasma oscillation frequency can be derived from (8) and can be described by a simple formula in the underdamped condiction as

$$f = \frac{1}{2\pi}\sqrt{\frac{Ne^2}{m_n\varepsilon} - \frac{\alpha_n^2}{4m_n^2}} \tag{27}$$

where $N$ is the carrier concentration. From (27), it is obvious that the plasma oscillation can only be observed when a small $\alpha_n$ is achieved. This corresponds to the situation of a weak total field, which will only occur with the saturated response.

Fig. 12 shows the corresponding transient electric field, electron velocity, and electron density distributions by neglecting the diffusion effect. We can find that the photocurrent oscillation observed in Fig. 11(a) is originated from the strong oscillations of the total electric field and the field-dependent electron velocity. This plasma oscillation can even affect the electron distribution as shown in Fig. 12(c). With the carrier diffusion considered, we can not observe similar strong oscillations in the electron velocity and density distributions shown in Figs. 8 and 9. The diffusion-considered $I_{\rm pd}$ and $I_r$ are also shown in Fig. 11(b) for comparison. Even though no strong oscillation is observed in the transient electron velocity and density distributions, we do still observe some small residual oscillation in $I_{\rm pd}$. The magnitude of the oscillation is smaller and the number of oscillation periods is also much less. This diffusion-suppressed plasma oscillation should thus be responsible for the negative electron velocity presented in Fig. 7(b).

### *F. Effect of Doping Density*

The discussion above is based on a doping density of $1\times10^{16}$ cm$^{-3}$ in the intrinsic region. We have also simulated the case for a higher intrinsic region doping density of $1 \times 10^{17}$ cm$^{-3}$. Instead of a flat bias field in the intrinsic region, a triangle shaped field is induced in this case with the electric field close to zero near the $p$ region. The condition for underdamped plasma oscillation should thus be easy established. Fig. 13 shows the simulated current response $I_{\rm pd}$ (dotted line) and the corresponding external circuit current response $I_r$ (dashed line) for a photocarrier concentration of $7 \times 10^{17}$ cm$^{-3}$ for the higher doping density case. Compared with the $I_{\rm pd}$ of the low-doping device in Fig. 11(b), we have observed a faster current quenching due to the lower setup threshold of the screening field. However, no photocurrent oscillation can be observed. We attribute this effect to the nonuniform distribution of the bias field. The underdamped plasma oscillations at different positions are created at different time delay with different phases. We thus can not observe any oscillation in the integrated current response. With

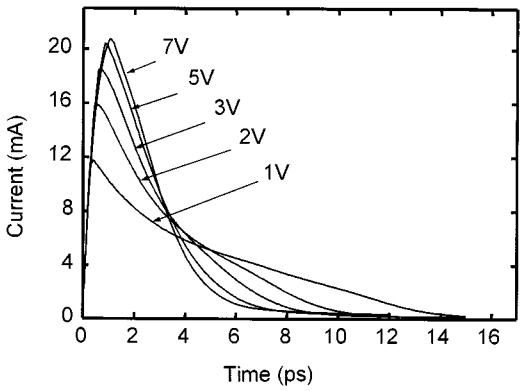


Fig. 10. Current responses $I_r$ under 1 V, 2 V, 3 V, 5 V, and 7 V reverse biases with trapping considered. The photocarrier concentrations are $7 \times 10^{17}$ cm$^{-3}$.

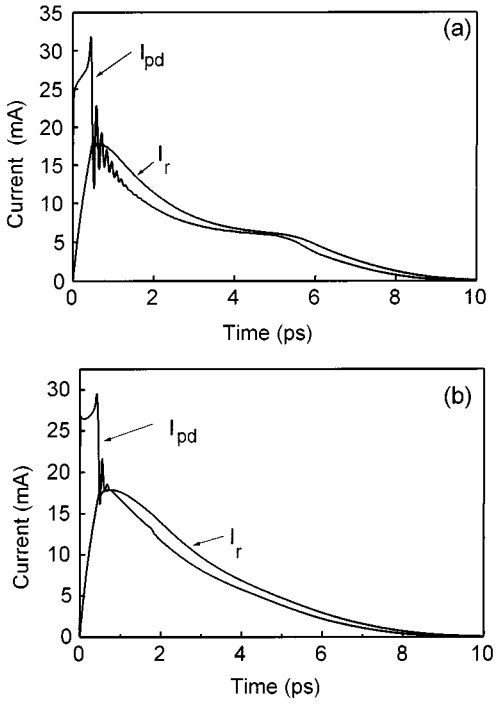


Fig. 11. External circuit current response $I_r$ and photodetector current response $I_{\rm pd}$ for a photocarrier concentration of $7 \times 10^{17}$ cm$^{-3}$ under a 2-V reverse bias with the carrier diffusion effect (a) neglected and (b) considered in the carrier trapping model.

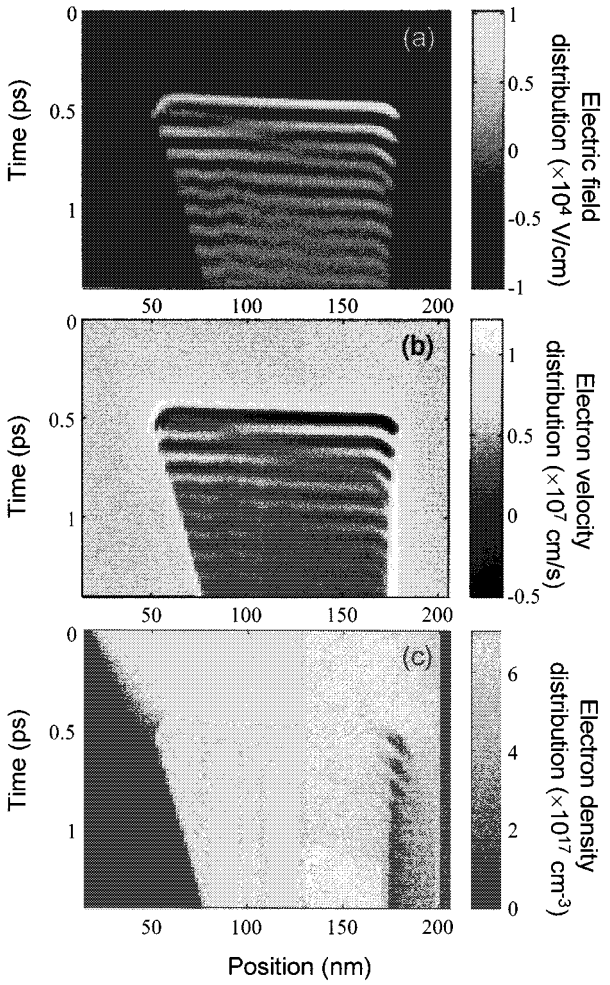


Fig. 12. (a) Transient total electric field distribution for a carrier concentration of $7 \times 10^{17}$ cm$^{-3}$ under a 2-V reverse bias with the carrier diffusion effect neglected in the carrier trapping model. (b) Corresponding transient electron velocity distribution. (c) Corresponding transient electron density distribution.

a faster field quenching, it is interesting to notice that the 3-dB bandwidth of the higher doping device does not decrease much, and the same 3-dB bandwidth of 51 GHz can be obtained for both doping cases.

## VI. Summary

We have simulated the nonlinear transport behaviors of an ultrahigh-speed p-i-n double-heterostructure photodetector, considering carrier transport, carrier trapping, and external circuit effects, including load resistance, device capacitance, and parasitic capacitance. In order to take into accounts of the influence of the carrier scattering and the strong electric field, we also consider the field-dependent and density-dependent effects on diffusion, damping, and carrier velocities. Under low illumination, device bandwidth is determined by carrier transit time and the RC time constant. Under high illumination, the nonlinear bandwidth saturation is found to be dominated not only by the drift-induced space charge effect, but also by the external circuit saturation and the carrier-trapping-induced space charge screening effects. Bias dependent current response is also studied. Higher bias will not only increase the threshold photocarrier density required to setup a space charge screening field,

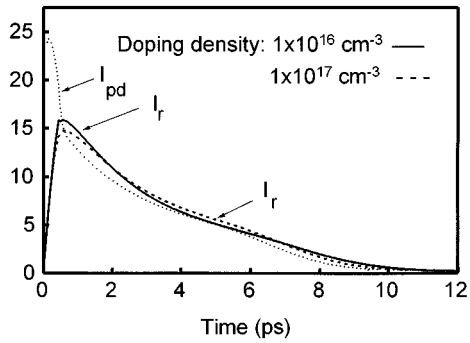


Fig. 13. The external circuit current responses $I_r$ (dashed line) and the photodetector current response $I_{\rm pd}$ (dotted line) for a higher doping density of $1 \times 10^{17}$ cm$^{-3}$. The photocarrier concentration is $7 \times 10^{17}$ cm$^{-3}$ with a 2-V reverse bias. $I_r$ with a lower doping density of $1 \times 10^{16}$ cm$^{-3}$ is also shown (solid line) for comparison.

but will also overcome the external circuit saturation. A gradual bandwidth recovery is thus observed when we increase the bias voltage. We have also studied the space charge field induced underdamped plasma oscillation. The underdamped plasma oscillation is responsible for the negative electron velocity observed in our simulation and is found to be greatly suppressed by the strong diffusion effect at room temperature. For a higher doping density in the intrinsic region, the oscillation becomes incoherent due to a triangle shaped bias field. However we do not find any strong influence of the device bandwidth by the doping density in the intrinsic region.

## Acknowledgment

The authors would like to thank the stimulating scientific discussions with J. E. Bowers, I.-H. Tan, K. Giboney, M. Rodwell, M. Pilkuhn, and U. K. Mishra.

## References

[1] J. E. Bowers and C. A. Burrus, "Ultrawide-band long-wavelength p-i-n photodetectors," *J. Lightwave Technol.*, vol. 5, pp. 1339–1350, Oct. 1987.

[2] Y. G. Wey, K. Giboney, J. E. Bowers, M. Rodwell, P. Silvestre, P. Thiagarajan, and G. Robinson, "110-GHz GaInAs/InP double heterostructure p-i-n photodetectors," *J. Lightwave Technol.*, vol. 13, pp. 1490–1499, July 1995.

[3] C.-K. Sun, I.-H. Tan, and J. E. Bowers, "Ultrafast transport dynamics of $p$-$i$-$n$ photodetectors under high-power illumination," *IEEE Photon. Technol. Lett.*, vol. 10, pp. 135–137, Jan. 1998.

[4] I.-H. Tan, C.-K. Sun, K. S. Giboney, J. E. Bowers, E. L. Hu, B. I. Miller, and R. J. Capik, "120 GHz long-wavelength low-capacitance photodetector with an air-bridged coplanar metal waveguide," *IEEE Photon. Technol. Lett.*, vol. 7, pp. 1477–1479, Dec. 1995.

[5] M. Dentan and B. De Cremoux, "Numerical simulation of the nonlinear response of a $p$-$i$-$n$ photodiode under high power illumination," *J. Lightwave Technol.*, vol. 8, pp. 1137–1144, Aug. 1990.

[6] D. G. Parker, "The theory, fabrication and assessment of ultra high speed photodiodes," *GEC, J. Res. Incorporating Marconi Rev.*, vol. 6, pp. 106–117, 1988.

[7] T. Ueda, K. Kusano, M. Sasaki, and M. Inoue, "Computer simulation of pulsed-laser induced coherent plasma oscillation in GaAs crystal," *J. Phys. Soc. Japan*, vol. 65, pp. 803–810, Mar. 1996.

[8] K. J. Williams, R. D. Esman, and M. Degenais, "Nonlinearities in $p$-$i$-$n$ microwave photodetectors," *J. Lightwave Technol.*, vol. 14, pp. 84–96, Jan. 1996.

[9] W. Sha and A. L. Smirl, "Coherent plasma oscillations in bulk semiconductors," *Phys. Rev. Lett.*, vol. 74, pp. 4273–4276, May 1995.

[10] S. Adachi, "Material parameter of $In_{1-x}Ga_x$ $As_yP_{1-y}$ and related binaries," *J. Appl. Phys.*, vol. 53, pp. 8775–8792, Dec. 1982.

[11] R. P. Joshi, A. M. Kriman, and D. K. Ferry, "Monte Carlo study of minority electronic transport in InGaAs: Effects of phonon mode splitting and dynamically screened electron-hole interaction," *J. Appl. Phys.*, vol. 68, pp. 4322–4324, Oct. 1990.
[12] T. H. Windhorn, L. W. Cook, and G. E. Stillman, "The electron velocity-field characteristic for $n$-$In_{0.53}Ga_{0.47}As$ at 300 K," *IEEE Electron Device Lett.*, vol. 3, pp. 18–20, Jan. 1982.
[13] M. A. Haase, V. M. Robbins, N. Tabatabaie, and G. E. Stillman, "Subthreshold electron velocity-field characteristics of GaAs and $In_{0.53}Ga_{0.47}As$," *J. Appl. phys.*, vol. 57, pp. 2295–2298, Mar. 1985.
[14] T. P. Pearsall and J. P. Hirtz, "The carrier mobilities in $Ga_{0.47}In_{0.53}As$ grown by organo-metallic CVD and liquid-phase epitaxy," *J. Crystal Growth*, vol. 54, pp. 127–131, 1981.
[15] B. R. Nag, S. R. Ahmed, and M. Deb Roy, "High-field autocovariance coefficient, diffusion coefficient and noise in InGaAs at 300 K," *Solid-State Electron.*, vol. 30, pp. 235–239, 1987.

**Yong-Liang Huang** was born in China in 1974. He received the B. S. degree in electrical engineering from the National Taiwan University, Taipei, R.O.C., in 1997 and the M. S. degree from Graduate Institute of Electro-Optical Engineering, National Taiwan University in 1999.

He is currently in the army for two years of military service.

**Chi-Kuang Sun** (M'96) was born in Tainan, Taiwan, R.O.C., on January 22, 1965. He received the B.S. degree in electrical engineering from National Taiwan University, Taipei, R.O.C., in 1987 and the M.S. and Ph.D. degrees in applied physics from Harvard University, Cambridge, MA, in 1990 and 1995, respectively.

He was a Visiting Scientist at the Research Laboratory of Electronics, Massachusetts Institute of Technology (MIT), Cambridge, between 1992 and 1994, working on femtosecond carrier dynamic studies of semiconductors and metals. He was with the NSF Center of Quantized Electronics Structures (QUEST) from 1995 to 1996 as an Assistant Research Engineer, conducting research on quantum dots, GaN, microcavity, high-speed communication devices and systems. He is now an associate professor in the Department of Electrical Engineering and Graduate Institute of Electro-Optical Engineering at National Taiwan University. His research interest are primarily concerned with femtosecond laser technology, high speed optoelectronics, ultrafast phenomena, novel quantum structures, GaN, and biomedical optics.

Dr. Sun is a member of the American Physical Society, the Optical Society of America (OSA), and the IEEE Laser and Electro-Optics Society (LEOS).